

Supporting Information for the Manuscript

Opening Magnetic Hysteresis *via* Improving Planarity of Equatorial Coordination by Hydrogen Bonding

Yun-Xia Qu, Ze-Yu Ruan, Bang-Heng Lyu, Yan-Cong Chen, Guo-Zhang Huang, Jun-Liang Liu* and Ming-Liang Tong*

Key Laboratory of Bioinorganic and Synthetic Chemistry of Ministry of Education, School of Chemistry, Sun Yat-Sen University, 510006 Guangzhou, Guangdong, P. R. China.

*Corresponding authors. Email: liujliang5@mail.sysu.edu.cn; tongml@mail.sysu.edu.cn.

Table of Contents

Part 1. Experimental Section.....	2
Part 2. Crystal Data and Structures.....	4
Part 3. Magnetic Characterization.....	9
Part 4. Photoluminescence Spectra.....	16
Part 5. <i>Ab initio</i> Calculations.....	19
Part 6. References.....	22

S1 Experimental Section

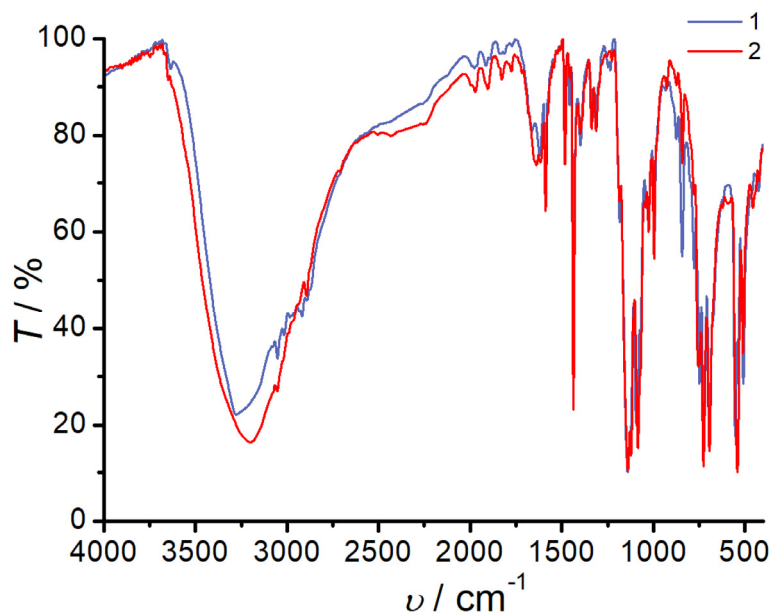


Fig S1. Infrared spectra for **1** (blue) and **2** (red).

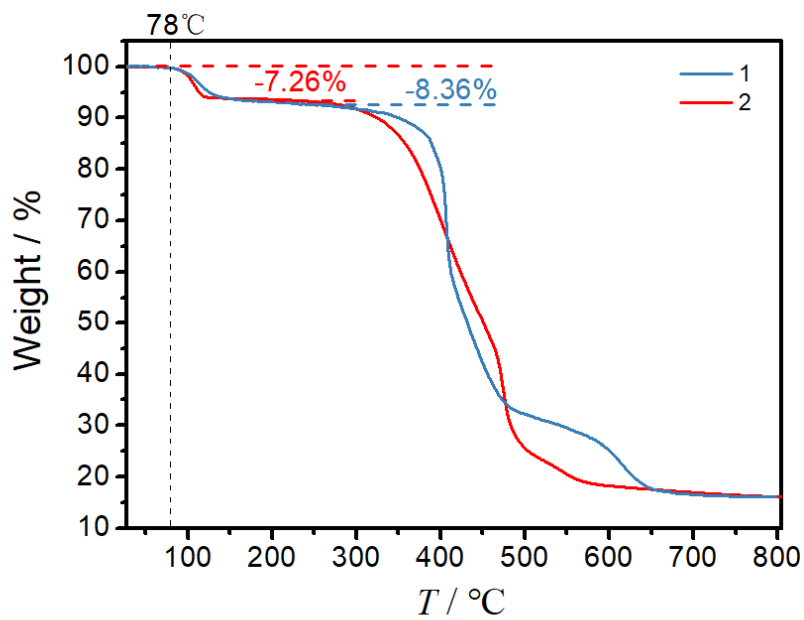


Fig S2. Thermogravimetric analysis for **1** (blue) and **2** (red) under N_2 atmosphere (10 K min⁻¹). The dashed lines correspond to the theoretical weight loss percentage of 1 EtOH plus 6 H_2O for **1** and 0.5EtOH plus 5.5 H_2O for **2**, respectively.

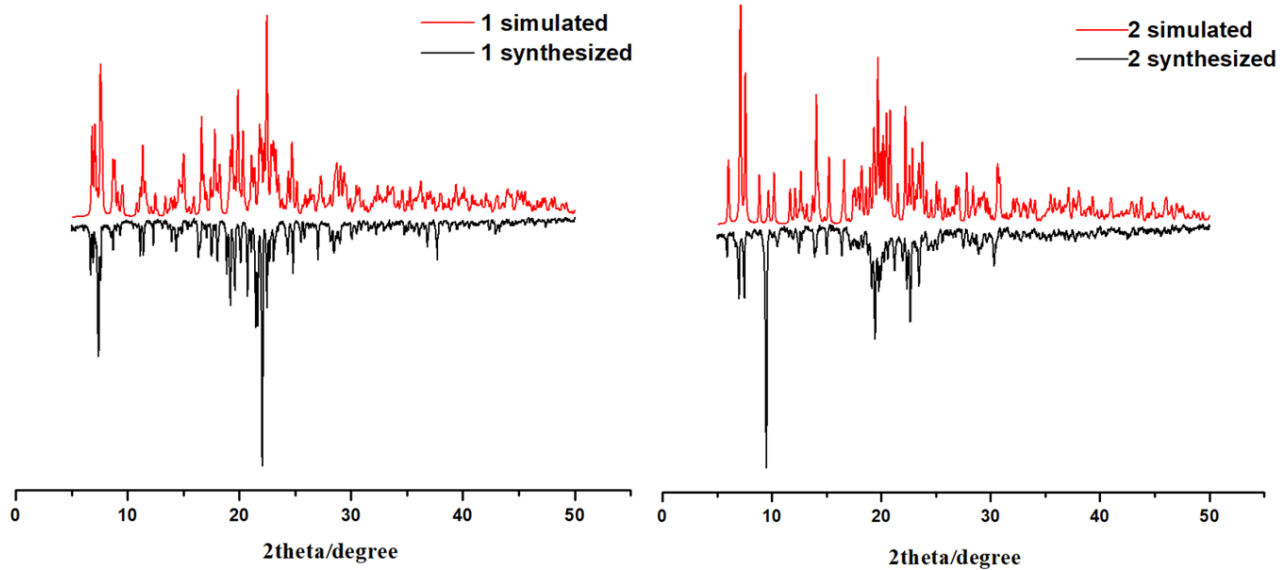


Fig S3. PXRD patterns of **1** (*left*) and **2** (*right*) compared with the simulated pattern from the single crystal structure.

Computational Details. All *ab initio* calculations were carried out with Open MOLCAS version 18.09¹ and are of the CASSCF/RASSI type. The Cholesky decomposition threshold was set to 1×10^{-8} to save disk space. Fragments of single-crystal structure of **1** and **2** were included, in which the butylene groups being replaced with ethyl groups, and the coordinates of atoms were extracted from the experimentally determined crystal structure. ANO-RCC-VTZP basis set have been employed for Dy atom, ANO-RCC-VDZP for O atoms, ANO-RCC-VDZ for C, P and I atoms and ANO-RCC-MB for H atoms.²⁻⁴ Active space of the CASSCF method included nine electrons in seven 4f orbitals of Dy^{III}. 21 sextets was optimized in state-averaged calculations, and then 21 sextets was mixed by spin-orbit coupling using RASSI approach.⁵ The g-tensors, energies, main magnetic axis as well as the magnetizations were obtained by SINGLE_ANISO routine.⁶

Magnetic Measurements

Magnetic susceptibility measurements were collected using a Quantum Design MPMS, MPMS3 and PPMS VSM magnetometer. Polycrystalline samples were embedded in vaseline to prevent torqueing. Alternating current (ac) magnetic susceptibility data measurements were performed with a 5 and 1.5 Oe oscillating field at frequencies between 0.1 or 1 to 999 or 1488 Hz. All data were corrected for the diamagnetic contribution.

S2 Crystal Data and Structures

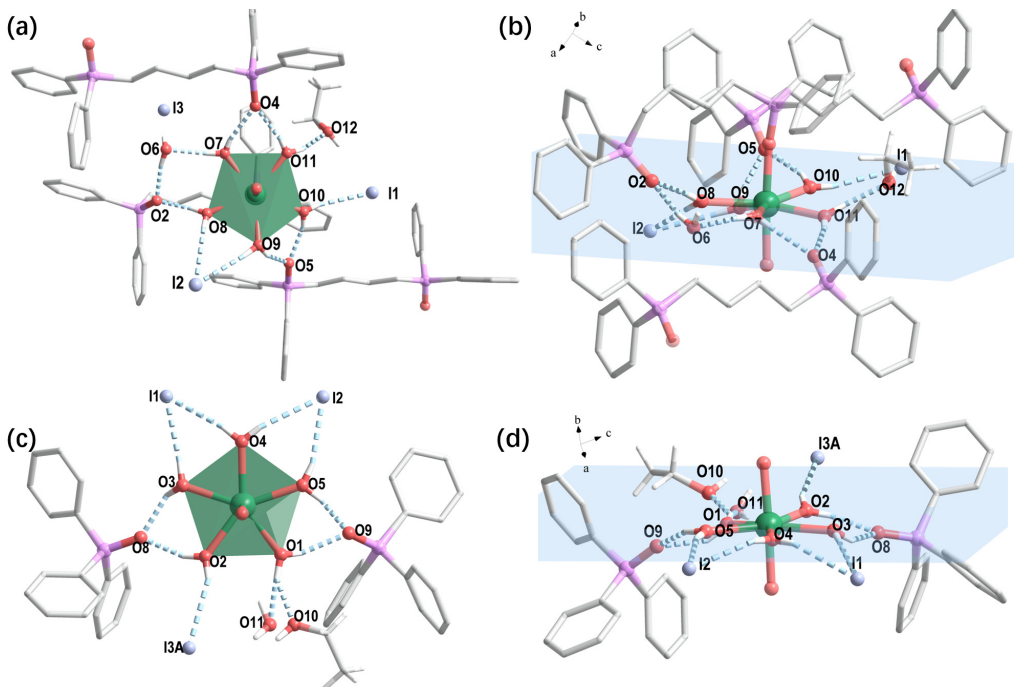


Fig. S4. The crystal structures with hydrogen bonds in **1** (a and b) and **2** (c and d). (a) and (c) are the top views of **1** and **2**, respectively. (b) and (d) are side views, where the blue plane is the least-square plane of equatorial-coordinate oxygen atoms. H atoms of the organic ligands and part of the axial-coordinate dppbO₂ ligands are omitted for clarity. Color code: Dy, green; O, red; P, lavender; C, grey; I, bluish violet; H, white.

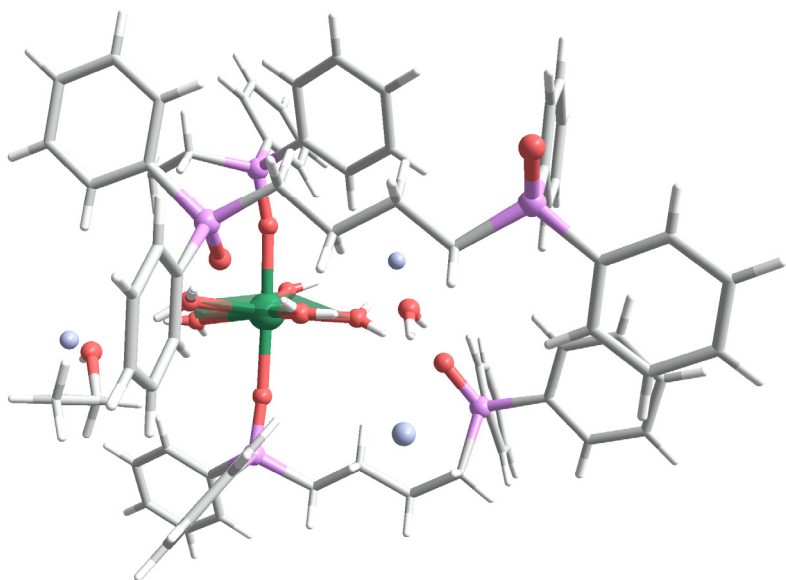


Fig S5. The asymmetric unit for **1**. Color code: Dy, green; O, red; P, lavender; C, grey; I, bluish violet; H, white.

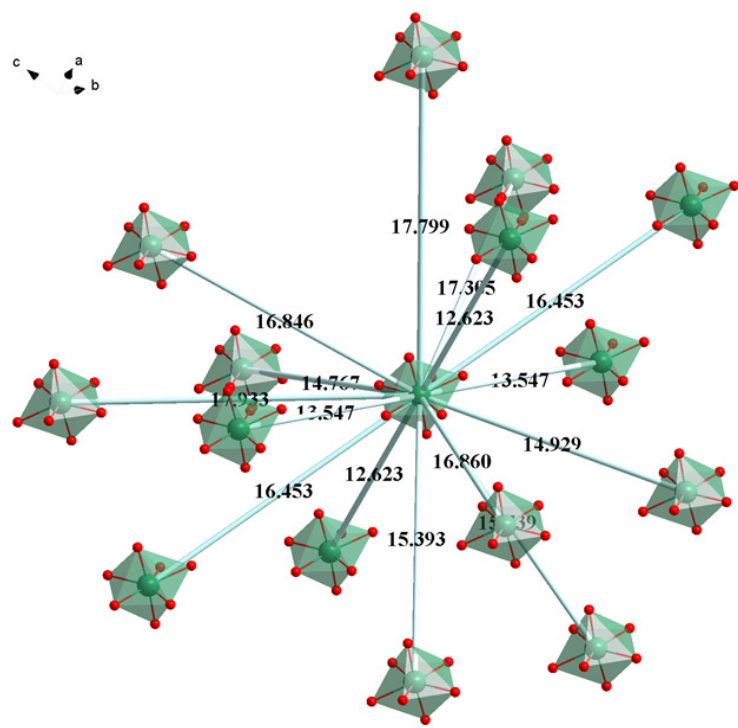


Fig S6. Dy-Dy distance between intermolecular for **1** with nearest distance is 12.6227(6) Å.

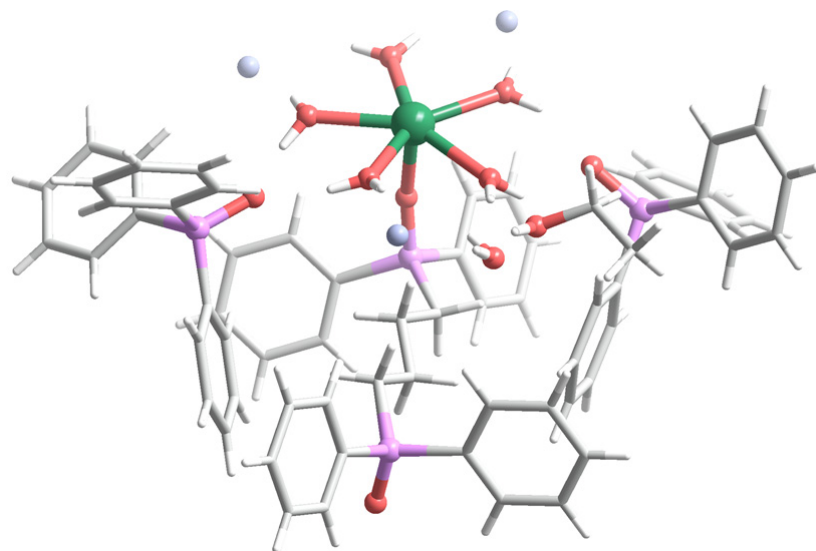


Fig S7. The asymmetric unit for **2**. Color code: Dy, green; O, red; P, lavender; C, grey; I, bluish violet; H, white.

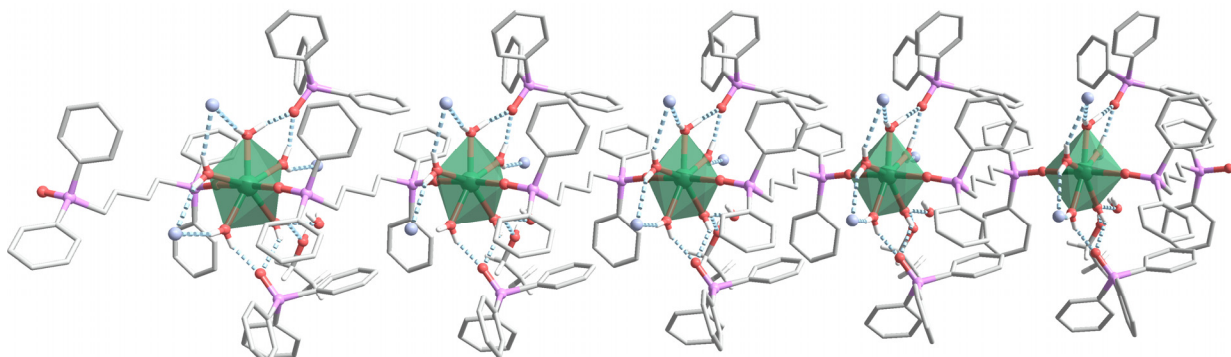


Fig S8. Crystal Structure of **2** viewed along the *b* axis. Color code: Dy, green; O, red; P, lavender; C, grey; I, bluish violet; H, white. H atoms of ligand are omitted for clarity.

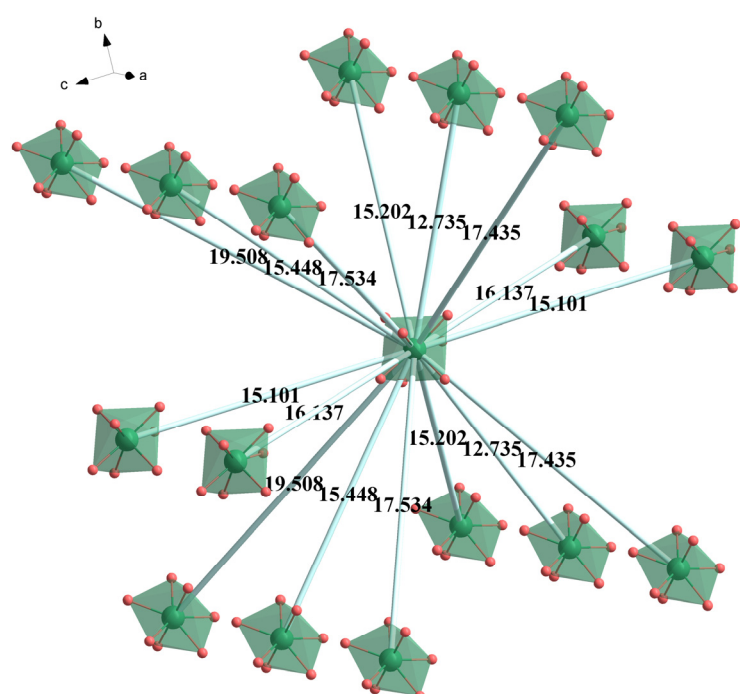


Fig S9. Dy-Dy distance between interchain for **2** with nearest distance is 12.7350(8) Å.

Table S1. Continuous Shape Measures calculations (CShM) for **1** and **2**.⁷

Complex	HP-7	HPY-7	HBPY-7	COC-7	CTPR-7	JPBPY-7	JETPY-7
	(D _{7h})	(C _{6v})	(D _{5h})	(C _{3v})	(C _{2v})	(D _{5h})	(C _{3v})
1	33.97234	23.21739	1.35508	4.19617	2.72181	4.08721	21.55288
2	34.07315	25.58438	0.31768	6.65599	5.11064	2.87612	22.89609

HP-7 = Heptagon; HPY-7 = Hexagonal pyramid; PBPY-7 = Pentagonal bipyramid; COC-7 = Capped octahedron; CTPR-7 = Capped trigonal prism; JPBPY-7 = Johnson pentagonal bipyramid J13; JETPY-7 = Johnson elongated triangular pyramid J7.

Table S2. Crystal data and structure refinement parameters for **1** and **2**

	1	2
Empirical formula	C ₇₂ H ₈₈ DyI ₃ O ₁₂ P ₅	C ₆₅ H ₇₂ DyI ₃ O ₁₀ P ₄
Formula weight	1843.47	1680.30
Temperature/K	120	120
Crystal system	triclinic	monoclinic
Space group	<i>P</i> -1	<i>P</i> 2 ₁
<i>a</i> /Å	12.6227(5)	10.2644(5)
<i>b</i> /Å	13.5467(5)	23.3768(11)
<i>c</i> /Å	23.6777(11)	15.1012(7)
<i>α</i> /°	100.264(2)	90
<i>β</i> /°	98.186(2)	103.623(2)
<i>γ</i> /°	102.180(2)	90
Volume/Å ³	3825.5(3)	3521.6(3)
<i>Z</i>	2	2
<i>ρ</i> _{calc} /g cm ⁻³	1.600	1.585
<i>μ</i> /mm ⁻¹	2.348	2.519
<i>F</i> (000)	1832	1654
Radiation	Mo- <i>Kα</i> (<i>λ</i> = 0.71073)	Mo- <i>Kα</i> (<i>λ</i> = 0.71073)
Reflections collected	66147	77697
Independent reflections	14046 [<i>R</i> _{int} = 0.0428, <i>R</i> _{sigma} = 0.0313]	16091 [<i>R</i> _{int} = 0.0451, <i>R</i> _{sigma} = 0.0387]
Goodness-of-fit on <i>F</i> ²	1.023	1.043
Final <i>R</i> indexes [<i>I</i> >=2σ(<i>I</i>)]	<i>R</i> ₁ = 0.0219, <i>wR</i> ₂ = 0.0429	<i>R</i> ₁ = 0.0242, <i>wR</i> ₂ = 0.0591
Final <i>R</i> indexes [all data]	<i>R</i> ₁ = 0.0319, <i>wR</i> ₂ = 0.0455	<i>R</i> ₁ = 0.0257, <i>wR</i> ₂ = 0.0596
Largest diff. peak/hole/eÅ ⁻³	0.38/-0.61	1.79/-0.89
Flack parameter	-	0.025(7)
CCDC no.	2063601	2063603

^a $R_1 = \sum |F_{\text{o}}| - |F_{\text{c}}| / \sum |F_{\text{o}}|$ ^b $wR_2 = \{[\sum w(F_{\text{o}}^2 - F_{\text{c}}^2)^2] / [\sum w(F_{\text{o}}^2)^2]\}^{1/2}$

Table S3. Selected bond lengths [Å] and angles [°] for **1** and **2**.

Bond lengths	1	Bond lengths	2	Bond angles	1	Bond angles	2
Dy-O1	2.2256(16)	Dy-O1	2.338(3)	O1-Dy1-O7	90.75(6)	O1-Dy1-O2	73.80(12)
Dy-O3	2.2163(16)	Dy-O2	2.359(3)	O1-Dy1-O8	88.69(7)	O1-Dy1-O3	143.95(12)
Dy-O7	2.3333(18)	Dy-O3	2.372(3)	O1-Dy1-O9	103.95(7)	O1-Dy1-O4	143.31(12)
Dy-O8	2.3688(19)	Dy-O4	2.386(3)	O1-Dy1-O10	81.27(7)	O1-Dy1-O5	72.04(12)
Dy-O9	2.3462(19)	Dy-O5	2.360(3)	O1-Dy1-O11	94.35(7)	O2-Dy1-O3	71.88(12)
Dy-O10	2.3693(19)	Dy-O6	2.210(3)	O3-Dy1-O1	174.74(6)	O2-Dy1-O4	142.75(12)
Dy-O11	2.3538(19)	Dy-O7 ¹	2.222(3)	O3-Dy1-O7	85.47(6)	O2-Dy1-O5	145.04(12)
				O3-Dy1-O8	93.79(7)	O3-Dy1-O4	71.14(12)
				O3-Dy1-O9	81.23(7)	O5-Dy1-O3	143.07(12)
				O3-Dy1-O10	99.86(7)	O5-Dy1-O4	71.98(12)
				O3-Dy1-O11	81.12(7)	O6-Dy1-O1	86.04(13)
				O7-Dy1-O8	74.27(7)	O6-Dy1-O2	94.40(12)
				O7-Dy1-O9	143.35(7)	O6-Dy1-O3	85.89(12)
				O7-Dy1-O10	145.93(7)	O6-Dy1-O4	87.30(13)
				O7-Dy1-O11	74.51(7)	O6-Dy1-O5	90.48(13)
				O8-Dy1-O10	137.95(7)	O6-Dy1-O7 ¹	177.75(14)
				O9-Dy1-O8	72.74(7)	O7 ¹ -Dy1-O1	93.36(13)
				O9-Dy1-O10	70.39(7)	O7 ¹ -Dy1-O2	87.51(12)
				O9-Dy1-O11	135.75(7)	O7 ¹ -Dy1-O3	95.84(12)
				O11-Dy1-O8	148.66(7)	O7 ¹ -Dy1-O4	91.90(12)
				O11-Dy1-O10	73.17(7)	O7 ¹ -Dy1-O5	87.28(13)

¹-1+x,+y,+z

S3 Magnetic Characterization

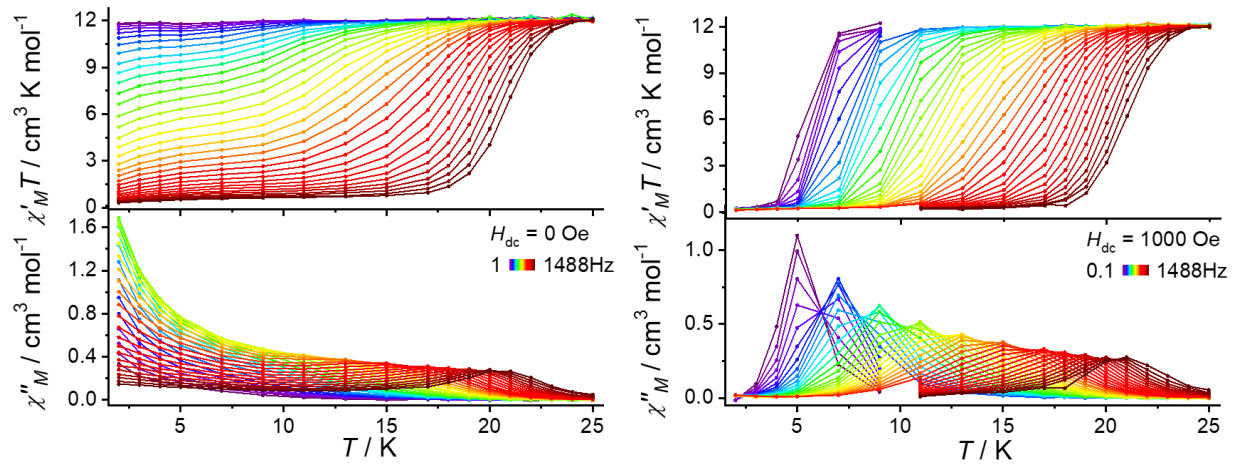


Fig S10. Temperature dependence of the in-phase ($\chi'_M T$) and out-of-phase (χ_M'') components of the ac magnetic susceptibility for **1** under 0 (*left*) and 1000 Oe (*right*) applied dc field with the ac frequency of 1-1488 and 0.1-1488 Hz as shown in the figure. Solid lines are guides to the eyes.

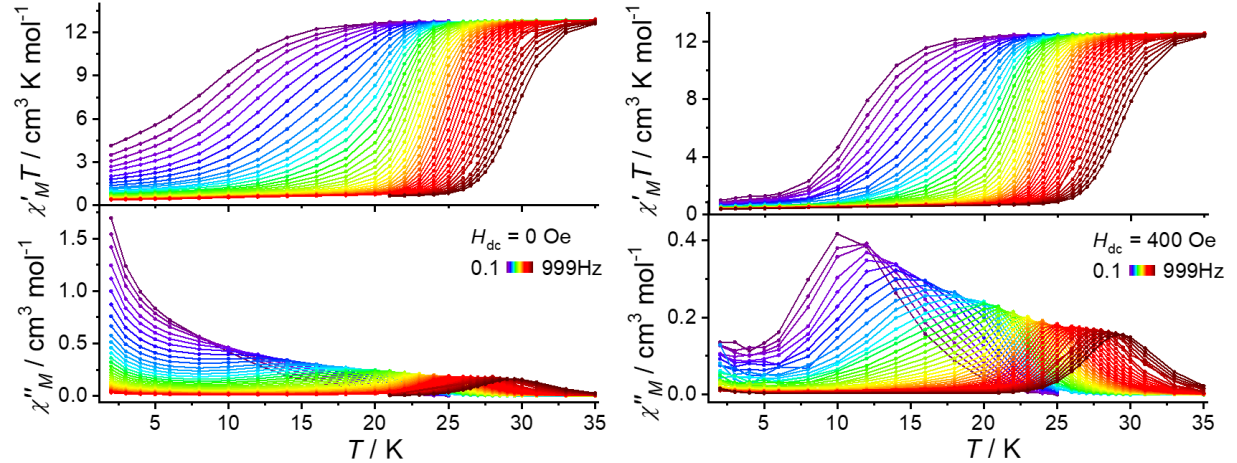


Fig S11. Temperature dependence of the in-phase ($\chi'_M T$) and out-of-phase (χ_M'') components of the ac magnetic susceptibility for **2** under 0 (*left*) and 400 Oe (*right*) applied dc field with the ac frequency of 0.1-999 Hz. Solid lines are guides to the eyes.

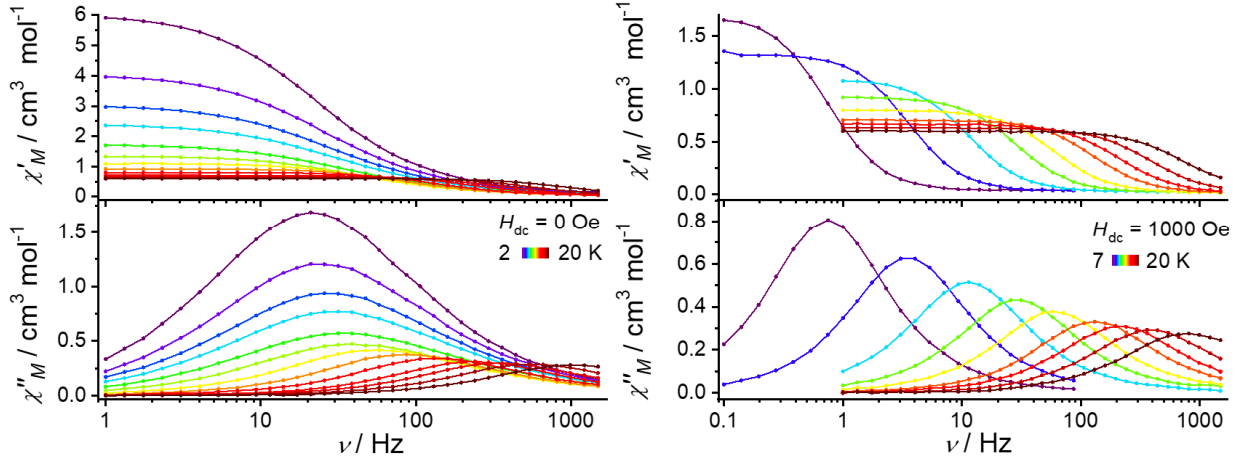


Fig S12. Frequency dependence in 0 and 1000 Oe dc field for **1**. Solid lines are guides to the eyes.

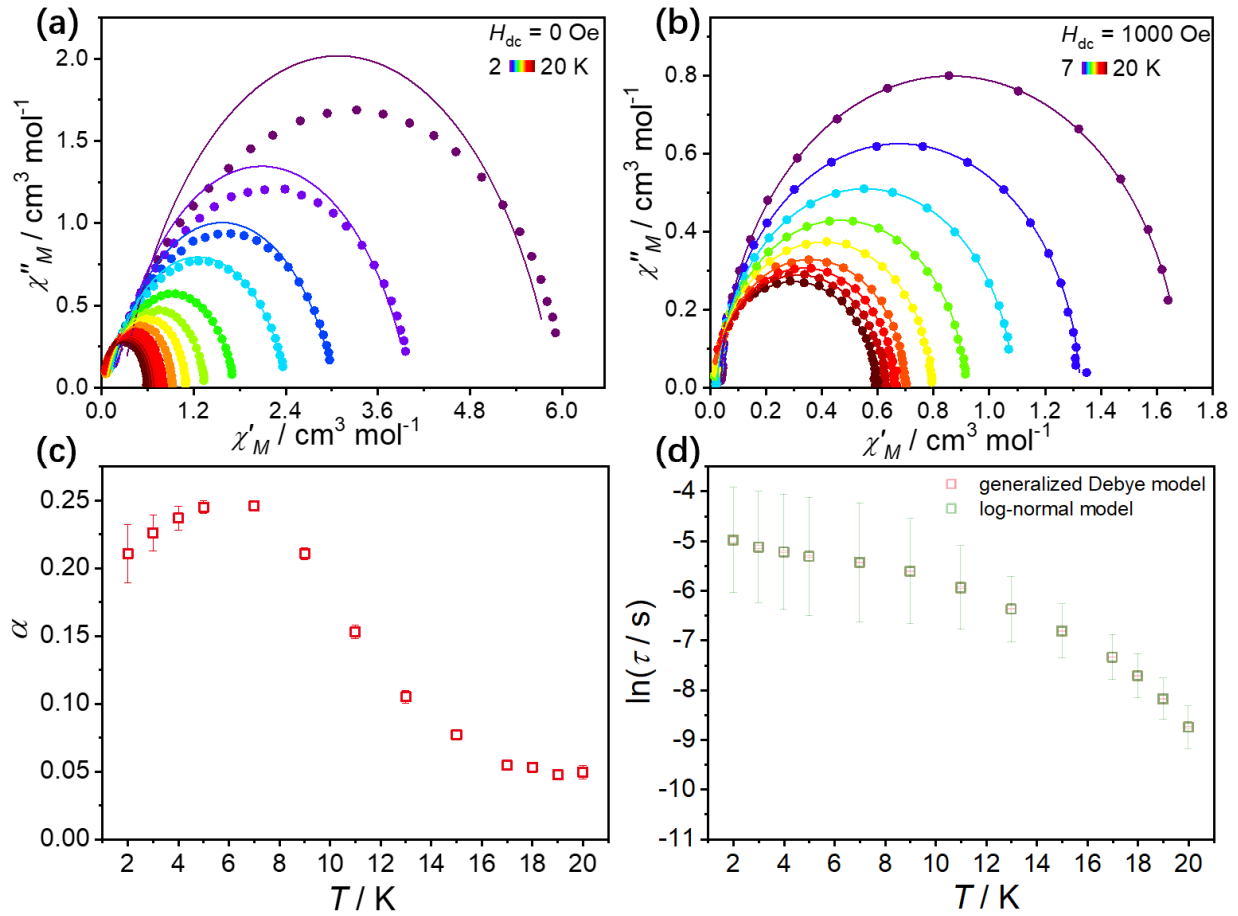


Fig S13. Cole–Cole plots of **1** at (a) 2–23 K under zero dc field and (b) 7–23 K under 1000 Oe dc field. Solid lines are best fits for the generalized Debye model. (c) α values obtained from the ac data under zero dc field with the generalized Debye model. (d) The relaxation times and their errors obtained from the ac data under zero dc field with the generalized Debye model (red) and the log-normal model (green).

Table S4. The fitting parameters of ac susceptibilities derived from the generalized Debye model for **1**

	T (K)	τ (s)	error (s)	χ_0 ($\text{cm}^3 \text{ mol}^{-1}$)	χ_∞ ($\text{cm}^3 \text{ mol}^{-1}$)	α	error
1 (0 Oe)	2	0.00686	3.16×10^{-4}	5.90937	0.25781	0.21084	0.02146
	3	0.00596	1.74×10^{-4}	4.02241	0.15228	0.22624	0.01334
	4	0.00541	1.05×10^{-4}	3.04139	0.10174	0.23717	0.00877
	5	0.00491	5.35×10^{-5}	2.43182	0.07446	0.24515	0.00487
	7	0.00437	3.24×10^{-5}	1.75906	0.0503	0.24604	0.00333
	9	0.00366	3.43×10^{-5}	1.37226	0.04865	0.21086	0.00448
	11	0.00263	2.54×10^{-5}	1.1156	0.04844	0.15318	0.00508
	13	0.00171	1.39×10^{-5}	0.93076	0.04311	0.10512	0.0046
	15	0.0011	7.19×10^{-6}	0.80496	0.03389	0.07721	0.00383
	17	6.49×10^{-4}	3.27×10^{-6}	0.70906	0.0281	0.05456	0.00298
	18	4.45×10^{-4}	2.48×10^{-6}	0.66815	0.02003	0.05317	0.00316
	19	2.81×10^{-4}	1.51×10^{-6}	0.63325	0.01292	0.04746	0.00277
	20	1.59×10^{-4}	2.02×10^{-6}	0.60164	0.(0055)	0.04957	0.00504
1 (1000 Oe)	7	0.2143	3.71×10^{-4}	1.69915	0.03798	0.01928	0.00105
	9	0.04532	1.52×10^{-4}	1.33439	0.03056	0.02088	0.00213
	11	0.01407	2.68×10^{-5}	1.09329	0.0243	0.02456	0.00115
	13	0.00551	1.81×10^{-5}	0.92081	0.01956	0.02556	0.00207
	15	0.00266	6.41×10^{-6}	0.79974	0.01717	0.02417	0.00153
	17	0.00122	3.93×10^{-6}	0.70606	0.01469	0.02624	0.00203
	18	7.46×10^{-4}	2.66×10^{-6}	0.66817	0.00987	0.03917	0.0022
	19	4.10×10^{-4}	1.73×10^{-6}	0.63315	0.00675	0.04556	0.0024
	20	2.05×10^{-4}	2.20×10^{-6}	0.60215	0.(0045)	0.05862	0.00474

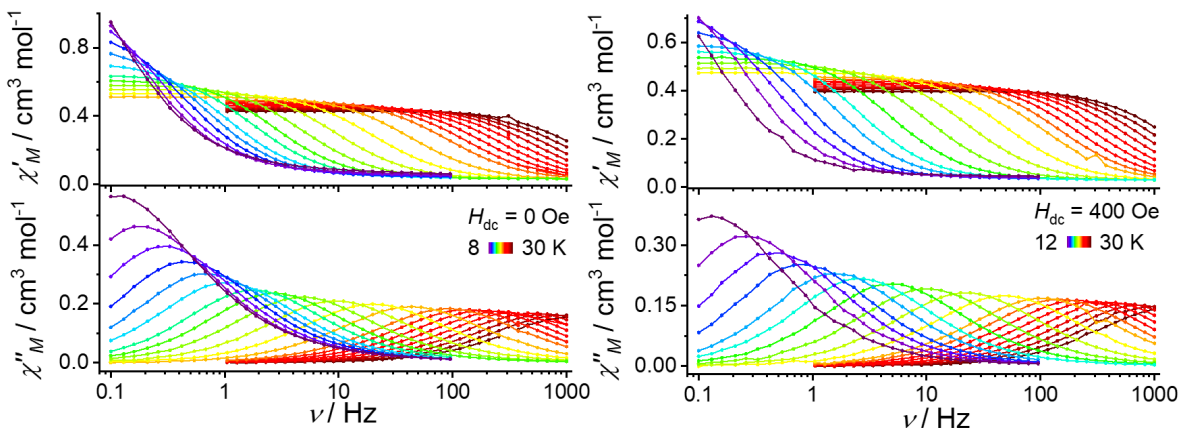


Fig S14. Frequency dependence in 0 and 400 Oe dc field for **2**. Solid lines are guides to the eyes.

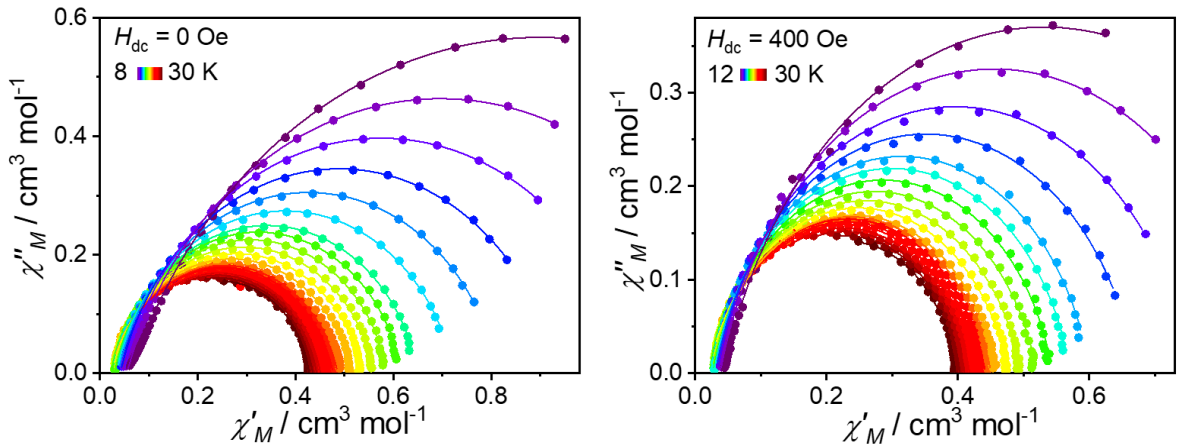


Fig S15. Cole–Cole plots of **2** at 8–30 K under zero dc field (*left*) and 12–30 K under 400 Oe dc field (*right*). Solid lines are best fits for the generalized Debye model.

Table S5. The fitting parameters of ac susceptibilities derived from the generalized Debye model for **2**

	T (K)	τ (s)	error (s)	χ_0 ($\text{cm}^3 \text{ mol}^{-1}$)	χ^∞ ($\text{cm}^3 \text{ mol}^{-1}$)	α	error
2 (0 Oe)	10	0.85963	0.00543	1.40891	0.05806	0.20283	0.0018
	12	0.53426	0.00191	1.16066	0.0506	0.17783	0.00132
	14	0.34081	0.00095	0.98724	0.0441	0.16359	0.00121
	16	0.22371	7.32×10^{-4}	0.85962	0.03936	0.1535	0.00156
	18	0.14864	5.25×10^{-4}	0.76327	0.03606	0.14563	0.0018
	20	0.0859	0.000404	0.68524	0.03375	0.13575	0.00252
	21	0.05579	2.44×10^{-4}	0.65025	0.03247	0.13141	0.00222
	22	0.03178	1.29×10^{-4}	0.61956	0.03071	0.1362	0.00206
	23	0.01618	7.15×10^{-5}	0.5917	0.02875	0.14356	0.00223
	24	0.00772	3.79×10^{-5}	0.56548	0.02664	0.14945	0.00246
	25	0.00361	1.76×10^{-5}	0.54264	0.0238	0.15433	0.0024
	26	0.00174	8.19×10^{-6}	0.5232	0.02368	0.15562	0.00241
	26.5	0.00122	6.28×10^{-6}	0.5125	0.02437	0.152	0.00263
	27	8.57×10^{-4}	4.32×10^{-6}	0.50283	0.02412	0.15054	0.00241
2 (400 Oe)	27.5	6.17×10^{-4}	3.46×10^{-6}	0.4933	0.02676	0.14486	0.00253
	28	4.65×10^{-4}	1.11×10^{-5}	0.48398	0.03331	0.13466	0.01006
	28.5	3.33×10^{-4}	2.66×10^{-6}	0.47528	0.03623	0.13035	0.00303
	29	2.52×10^{-4}	2.49×10^{-6}	0.46694	0.04378	0.12245	0.00333
	29.5	1.93×10^{-4}	2.56×10^{-6}	0.45879	0.05291	0.11366	0.00395
	30	1.56×10^{-4}	2.22×10^{-6}	0.45082	0.07206	0.09309	0.00396
	10	3.09819	0.13733	1.35053	0.05335	0.21584	0.00611
	12	1.1749	0.01698	1.07571	0.04606	0.17454	0.00383
	14	0.58396	0.00301	0.92031	0.04024	0.15744	0.00195
	16	0.32385	0.00174	0.80008	0.03571	0.15203	0.00241

18	0.18831	0.00102	0.70796	0.03308	0.14205	0.0027
20	0.09567	5.01×10^{-4}	0.63346	0.03149	0.13181	0.00281
21	0.05844	2.30×10^{-4}	0.60213	0.03012	0.13558	0.00199
22	0.03129	1.49×10^{-4}	0.57377	0.02868	0.14219	0.00241
23	0.01517	7.70×10^{-5}	0.5483	0.02654	0.15258	0.00253
24	0.00699	3.54×10^{-5}	0.52365	0.02428	0.15782	0.0025
25	0.00323	1.70×10^{-5}	0.50285	0.02221	0.16066	0.00256
26	0.00156	1.95×10^{-5}	0.48515	0.02404	0.16224	0.00628
26.5	0.00108	5.61×10^{-6}	0.47512	0.02211	0.15819	0.00253
27	7.62×10^{-4}	4.53×10^{-6}	0.46619	0.02225	0.15482	0.00275
27.5	5.51×10^{-4}	3.68×10^{-6}	0.45719	0.02607	0.14802	0.0029
28	4.07×10^{-4}	4.41×10^{-6}	0.44876	0.03096	0.13821	0.00437
28.5	3.01×10^{-4}	2.98×10^{-6}	0.44057	0.03699	0.13275	0.00355
29	2.30×10^{-4}	2.79×10^{-6}	0.43269	0.04604	0.12147	0.00391
29.5	1.82×10^{-4}	3.44×10^{-6}	0.42526	0.05931	0.10593	0.00552
30	1.43×10^{-4}	2.87×10^{-6}	0.41805	0.07158	0.09812	0.00511

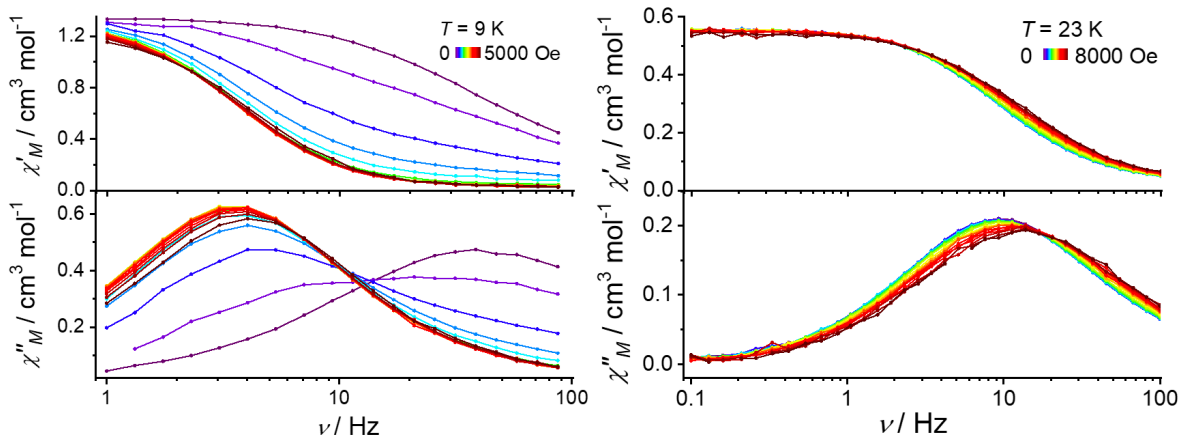


Fig S16. Field dependence of the alternating-current molar magnetic susceptibilities for **1** at 9 K (*left*) and **2** at 23 K (*right*), respectively. Solid lines are guides to the eyes.

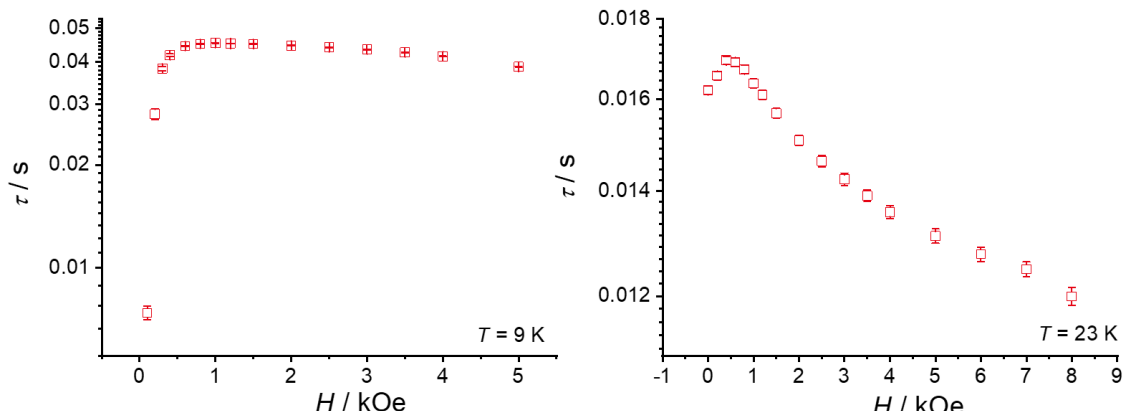


Fig S17. Field dependence of the relaxation time for **1** (*left*) and **2** (*right*).

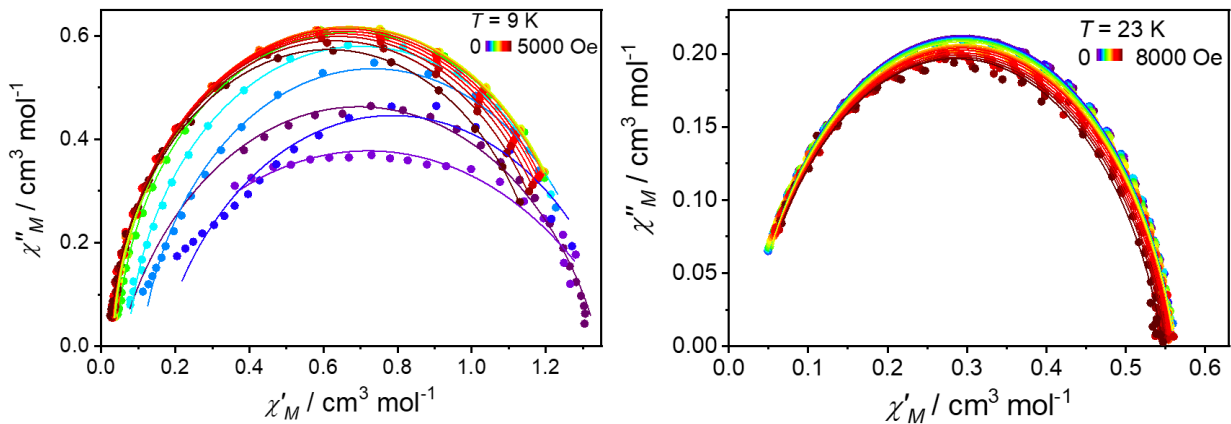


Fig S18. Cole-Cole plots of **1** (*left*) at 9 K under 0-5000 Oe dc field and **2** (*right*) at 23 K under 0-8000 Oe dc field, and solid lines are best fits for the generalized Debye model.

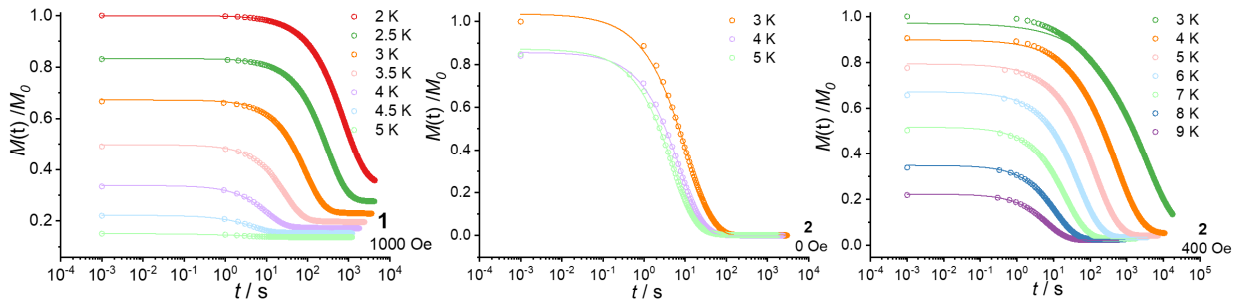


Fig S19. DC magnetization decay of **1** and **2** with final field as shown. The magnetic field was ramped to 2 T for **1** and 3 T for **2** and then the temperature was declined to the indicated temperature. After temperature and magnetic moment are steady, the magnetic field was started to reach 1000 Oe for **1**, 0 and 400 Oe for **2**, and kept unchanged for at least $10^3 \sim 10^4$ s depending on the measured temperature. During the procedure, the magnetization kept measuring. The solid lines are the best fit to the exponential decay as $M(t) = M_f + (M_i - M_f) \exp[-(t/\tau)^\beta]$, where τ is the relaxation time.

Table S6. The fitting parameters of dc magnetization decay derived from $M(t) = M_f + (M_i - M_f) \exp[-(t/\tau)^\beta]$ for **1** with final field of 1000 Oe and **2** with final field of 0 and 400 Oe, respectively.

	T (K)	M_f (emu)	M_i (emu)	τ (s)	error (s)	β	error
1 (1000 Oe)	2	0.0559	0.16149	791.96194	0.08529	0.82671	1.20125×10^{-4}
	2.5	0.04467	0.13458	308.73248	0.08181	0.89268	2.40463×10^{-4}
	3	0.03708	0.1086	88.97777	0.09574	0.91257	9.73445×10^{-4}
	3.5	0.03168	0.08033	28.23852	0.07129	0.91123	0.00228
	4	0.02769	0.05447	10.65093	0.04486	0.88009	0.0036
	4.5	0.0246	0.0358	4.95725	0.039	0.82818	0.00613
	5	0.02214	0.02436	3.10501	0.06876	0.55841	0.00737
2 (0 Oe)	3	3.35645×10^{-5}	0.04104	11.24995	0.02364	0.69221	9.96993×10^{-4}
	4	1.83643×10^{-5}	0.03394	7.42866	0.0126	0.76638	0.00106

	5	8.22918×10^{-5}	0.03455	5.11584	0.00917	0.75801	0.00107
2 (400 Oe)	3	0.00441	0.09812	3145.30655	2.05749	0.4855	3.33245×10^{-4}
	4	0.00532	0.09077	493.00595	0.1003	0.60324	7.65741×10^{-5}
	5	0.0043	0.08017	135.30055	0.02988	0.66398	9.10725×10^{-5}
	6	0.00358	0.06792	48.68896	0.02032	0.70439	1.97618×10^{-4}
	7	0.00307	0.05233	21.84279	0.01289	0.74151	3.16805×10^{-4}
	8	0.00269	0.03522	11.74531	0.01216	0.78361	6.44242×10^{-4}
	9	0.00238	0.02258	6.83429	0.00814	0.80736	8.09933×10^{-4}

S4 Photoluminescence Spectra

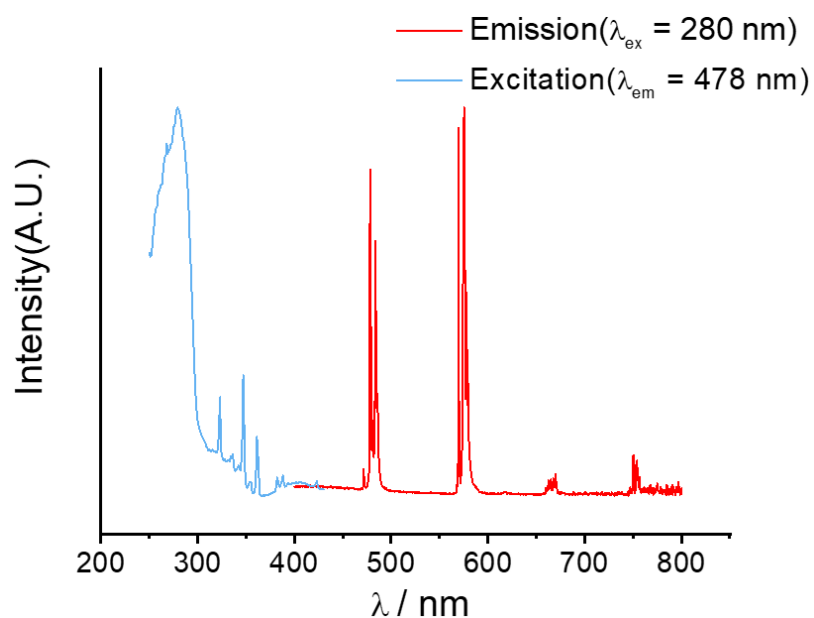


Fig S20. Photoluminescence spectra for **1** at 6 K.

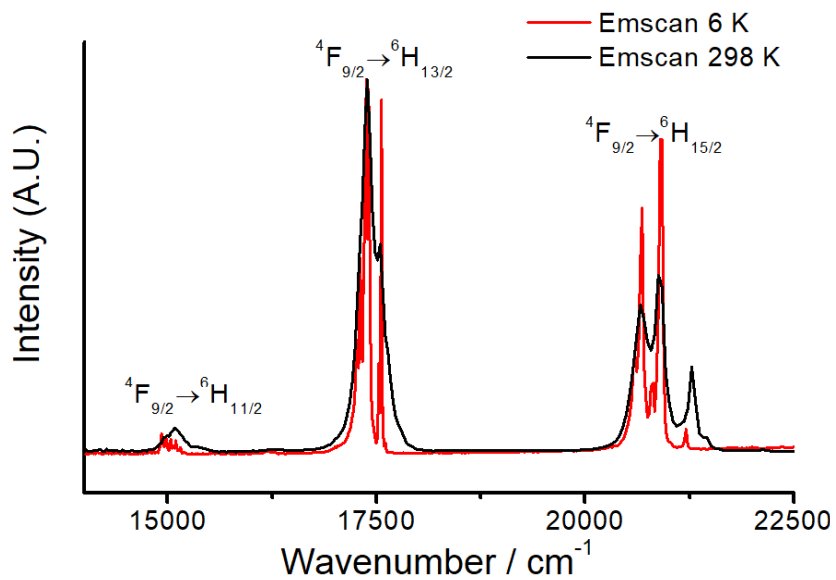


Fig S21. The emission spectra were measured at 298 K ($\lambda_{\text{ex}} = 292 \text{ nm}$) and 6 K ($\lambda_{\text{ex}} = 280 \text{ nm}$) for **1**.

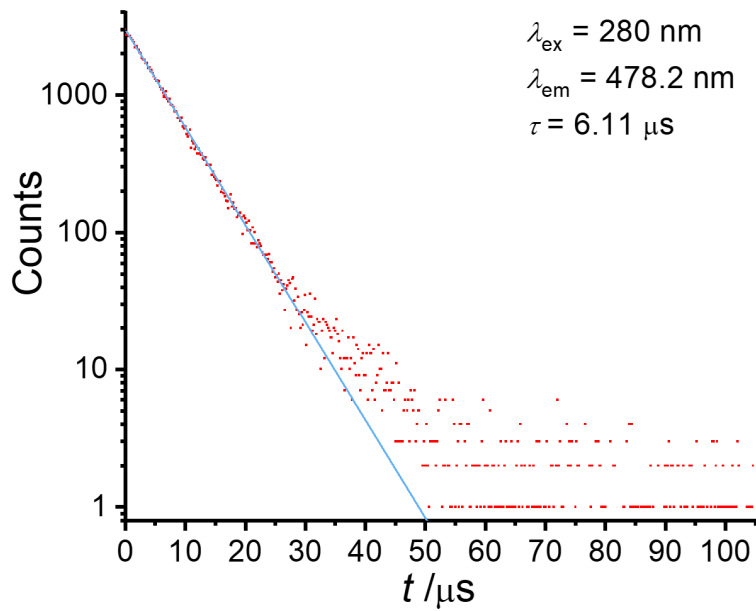


Fig S22. Lifetime measurements were collected at 6 K with mean lifetime $\tau = 6.11(1) \mu\text{s}$ (by first order exponential fits) for **1**.

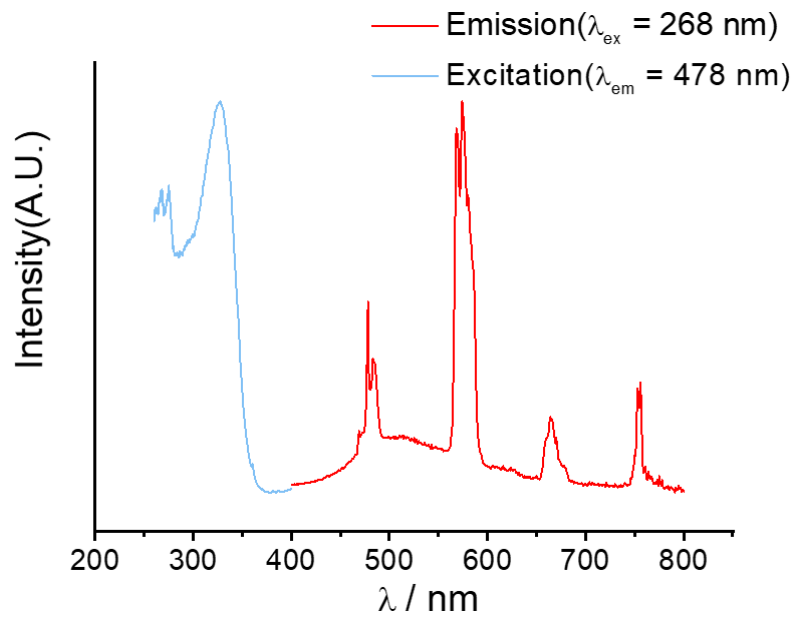


Fig S23. Photoluminescence spectra for **2** at 11 K.

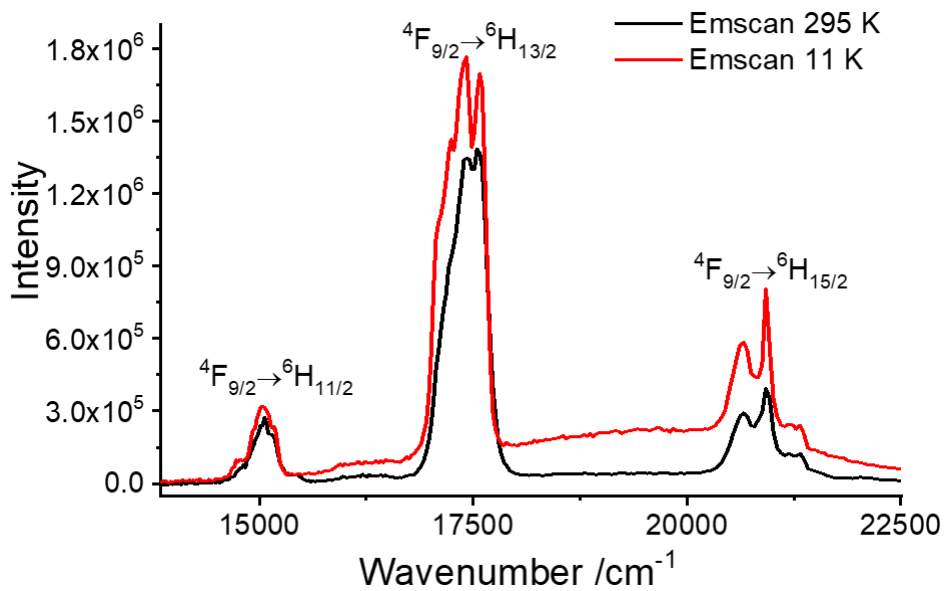


Fig S24. The emission spectra were measured at 295 K and 11 K when $\lambda_{\text{ex}} = 276$ nm for **2**.

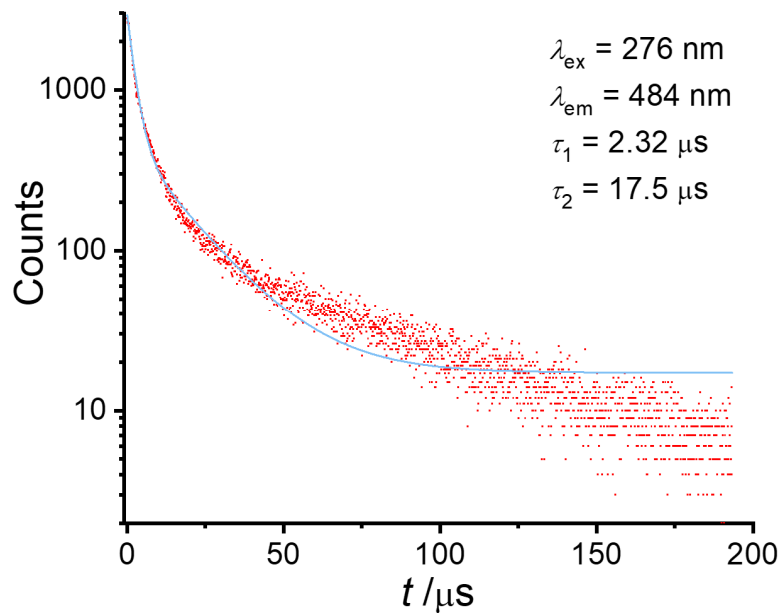


Fig S25. Lifetime measurements were collected at 10 K with mean lifetime $\tau_1 = 2.32(2)$, $\tau_2 = 17.5(3)$ μs (by second order exponential fits) for **2**.

S5 *Ab initio* Calculations

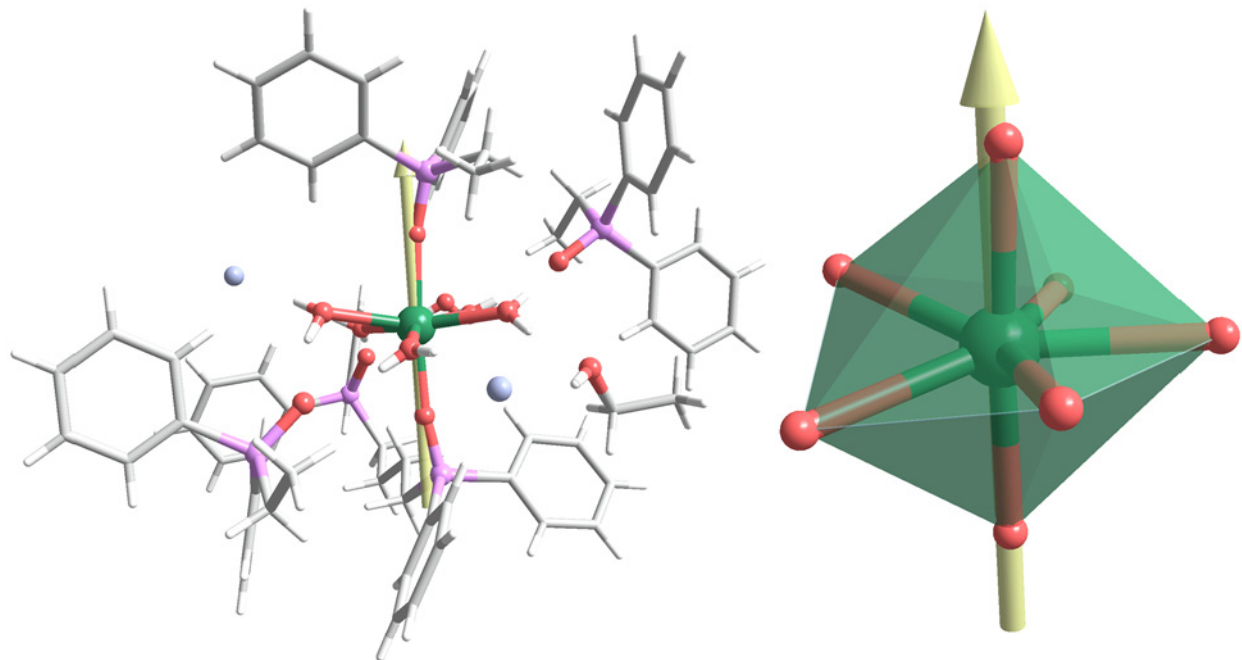


Fig S26. The fragment of single-crystal structure of **1** used for the *ab initio* calculations (*left*), where the main magnetic axis of the ground Kramers doublet (yellow arrow) is virtually along the pair of phosphine oxide ligand' oxygen atoms. The central Dy displays pentagonal bipyramidal geometry with the orientation of the main magnetic axis (*right*).

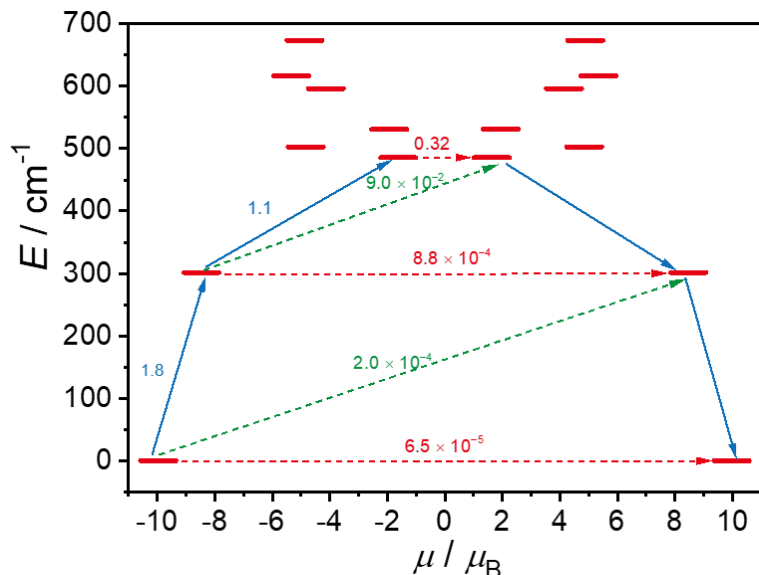


Fig S27. Magnetization blocking barriers for dimer **1**. The lowest 16 spin-orbit states are arranged according to the magnitude of their magnetic moments on the horizontal axis. The numbers next to arrows connecting two states display the average transition magnetic moment matrix element between the respective states.

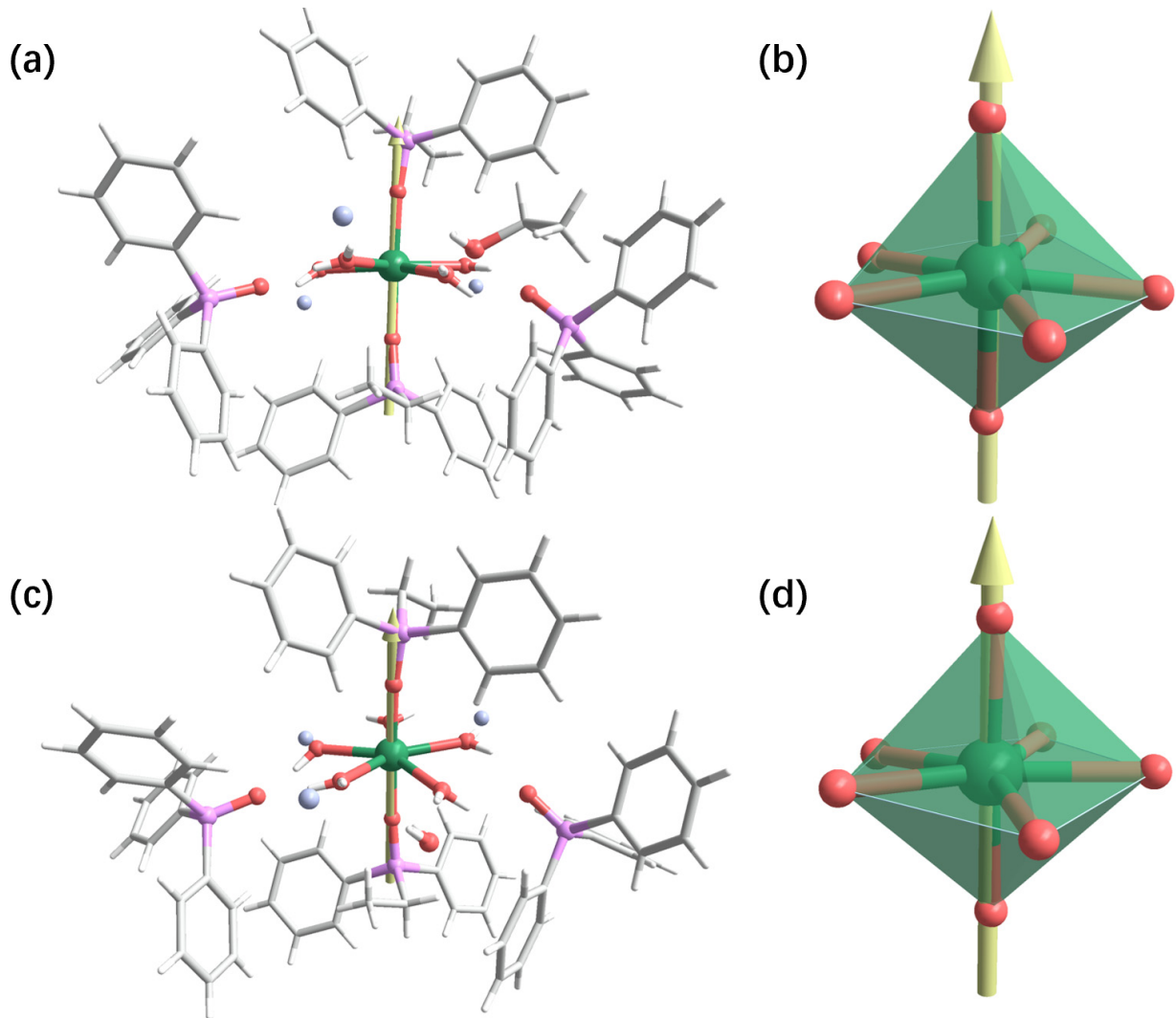


Fig S28. The fragment of single-crystal structure of **2** used for the model A1 (a) and A2 (c) *ab initio* calculations, where the main magnetic axis of the ground Kramers doublet (yellow arrow) is virtually along the pair of phosphine oxide ligand' oxygen atoms. The central Dy displays pentagonal bipyramidal geometry with the orientation of the main magnetic axis for model A1 (b) and A2 (d), respectively.

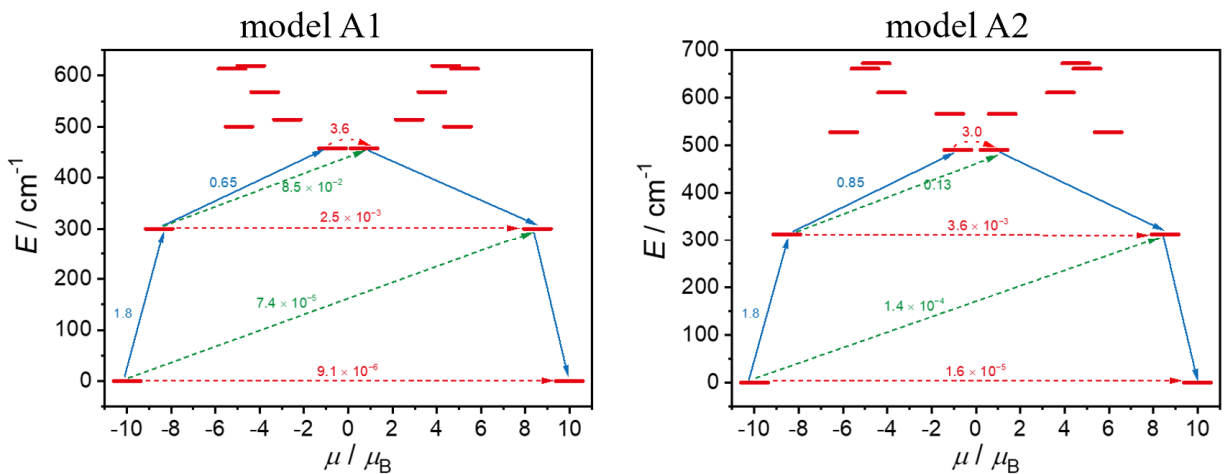


Fig S29. Magnetization blocking barriers for polymer **2** by model A1 (*left*) and A2 (*right*), respectively. The

lowest 16 spin-orbit states are arranged according to the magnitude of their magnetic moments on the horizontal axis. The numbers next to arrows connecting two states display the average transition magnetic moment matrix element between the respective states.

Table S5. Energy (cm^{-1}), magnetic anisotropy of the low-lying energy states arising from the ligand field splitting of the ground manifold $J = 15/2$ and angles ($^\circ$) between the main magnetic axes of the selected Kramers doublet and the ground Kramers doublet for the local Dy^{III} site in **1** and **2**, obtained in the *ab initio* calculations.

KD	1			2-model A1			2- model A2		
	E / cm^{-1}	g	Angle / $^\circ$	E / cm^{-1}	g	Angle / $^\circ$	E / cm^{-1}	g	Angle / $^\circ$
1	0	0.0002	0	0	0.0000	0	0	0.0000	0
		0.0002			0.0000			0.0001	
		19.935			19.970			19.966	
2	301.833	0.0018	1.1406	300.282	0.0071	0.5035	312.877	0.0096	0.6762
		0.0035			0.0081			0.0123	
		16.929			17.078			17.068	
3	485.417	2.7683	88.728	457.700	1.2824	87.824	490.532	1.4099	87.381
		5.7813			3.3984			1.6489	
		12.877			16.752			17.683	
4	502.673	0.6269	1.0010	500.022	1.4018	17.271	527.647	0.2407	4.9332
		4.1862			2.5978			2.3078	
		9.6789			10.316			11.970	
5	530.928	3.6260	78.669	513.874	2.8639	58.817	566.364	9.9856	11.979
		5.3479			4.4698			7.1253	
		7.0727			8.9317			1.8891	
6	596.164	0.2175	32.291	567.586	0.3789	25.444	610.829	2.7717	40.213
		3.0177			1.3328			3.4304	
		9.7420			8.3597			9.6813	
7	616.640	0.4964	38.107	613.501	1.4608	10.945	661.184	0.0818	47.450
		2.0483			4.6183			1.0672	
		13.526			10.686			14.764	
8	673.490	0.0014	58.196	619.324	9.4504	68.998	672.063	0.1081	50.673
		0.1686			5.3497			1.3091	
		18.521			0.6632			14.138	

S6 References

- 1 F. Aquilante, J. Autschbach, R. K. Carlson, L. F. Chibotaru, M. G. Delcey, L. De Vico, I. Fdez. Galván, N. Ferré, L. M. Frutos, L. Gagliardi, M. Garavelli, A. Giussani, C. E. Hoyer, G. Li Manni, H. Lischka, D. Ma, P. Å. Malmqvist, T. Müller, A. Nenov, M. Olivucci, T. B. Pedersen, D. Peng, F. Plasser, B. Pritchard, M. Reiher, I. Rivalta, I. Schapiro, J. Segarra-Martí, M. Stenrup, D. G. Truhlar, L. Ungur, A. Valentini, S. Vancoillie, V. Veryazov, V. P. Vysotskiy, O. Weingart, F. Zapata and R. Lindh, Molcas 8: New capabilities for multiconfigurational quantum chemical calculations across the periodic table. *J. Comput. Chem.*, 2016, **37**, 506-541.
- 2 B. O. Roos, R. Lindh, P.-Å. Malmqvist, V. Veryazov, P.-O. Widmark and A. C. Borin, New relativistic atomic natural orbital basis sets for lanthanide atoms with applications to the Ce diatom and LuF₃. *J. Phys. Chem. A.*, 2008, **112**, 11431-11435.
- 3 B. O. Roos, R. Lindh, P.-Å. Malmqvist, V. Veryazov and P.-O. Widmark, Main group atoms and dimers studied with a new relativistic ANO basis set. *J. Phys. Chem. A.*, 2004, **108**, 2851-2858.
- 4 B. O. Roos, R. Lindh, P.-Å. Malmqvist, V. Veryazov and P.-O. Widmark, New relativistic ANO basis sets for transition metal atoms. *J. Phys. Chem. A.*, 2005, **109**, 6575-6579.
- 5 P. Å. Malmqvist, B. O. Roos and B. Schimmelpfennig, The restricted active space (RAS) state interaction approach with spin-orbit coupling. *Chem. Phys. Lett.*, 2002, **357**, 230-240.
- 6 L. F. Chibotaru and L. Ungur, *Ab initio* calculation of anisotropic magnetic properties of complexes. I. Unique definition of pseudospin hamiltonians and their derivation. *J. Chem. Phys.*, 2012, **137**, 064112.
- 7 (a) Casanova, D.; Cirera, J.; Llunell, M.; Alemany, P.; Avnir, D.; Alvarez, S., Minimal Distortion Pathways in Polyhedral Rearrangements. *J. Am. Chem. Soc.*, 2004, **126** (6), 1755-1763. (b) D. Casanova, M. Llunell, P. Alemany and S. Alvarez, The rich stereochemistry of eight-vertex polyhedra, A continuous shape measures study. *Chem. Eur. J.*, 2005, **11**, 1479-1494. (c) S. Alvarez, P. Alemany, D. Casanova, J. Cirera, M. Llunell and D. Avnir, Shape maps and polyhedral interconversion paths in transition metal chemistry. *Coord. Chem. Rev.*, 2005, **249**, 1693-1708. (d) Cirera, J.; Ruiz, E.; Alvarez, S., Shape and Spin State in Four-Coordinate Transition-Metal Complexes: The Case of the d6 Configuration. *Chem. Eur. J.*, 2006, **12** (11), 3162-3167.